

## Flat and curved crystal spectrography for mammographic X-ray sources

<sup>1,2</sup>C T CHANTLER, BSc, DPhil, <sup>2</sup>R D DESLATTES, BSc, PhD, <sup>2</sup>A HENINS, BSc, PhD and <sup>2</sup>L T HUDSON, BSc, MSc, PhD

<sup>1</sup>School of Physics, University of Melbourne, Parkville, Victoria 3052, Australia, and <sup>2</sup>National Institute of Standards and Technology, Gaithersburg, Maryland 20899, USA

### Abstract

The demand for improved spectral understanding of mammographic X-ray sources and non-invasive voltage calibration of such sources has led to research into applications using curved crystal spectroscopy. Recent developments and the promise of improved precision and control are described. Analytical equations are presented to indicate effects of errors and alignment problems in the flat and curved crystal systems. These are appropriate for all detection systems. Application to and testing of spectrographic detection (using standard X-ray film) is presented. Suitable arrangements exist which can be used to measure X-ray tube voltages well below 1 kV precision in the operating range of 20–35 kV.

Department of Health (UK) guidelines require that the indicated voltage on X-ray generating equipment for mammography should be correct to within 1 kV [1, 2]. Smaller changes have been demonstrated to have effects on image quality (and, of course, on patient dosage). To avoid adverse effects, control and calibration procedures should determine any such operating parameter to significantly better than the nominal requirement. In this case, a tolerance of better than 0.5 kV in absolute accuracy, across the operating range of 20–35 kV, might be appropriate. Requirements relate to precision and reproducibility as well as to absolute accuracy. The precision of a result will normally be significantly better than the accuracy.

Although the applied high voltage can be measured by traditional (invasive) high voltage (HV) divider techniques with more than adequate precision for the case of well-filtered DC potentials, sources used in mammography are normally not readily or appropriately investigated by such means. Consequently, there has been a proliferation of non-invasive techniques, which seek to establish a voltage estimate on the basis of penetration of the generated radiation through two or more absorbers. Such devices are dependent on any prior filtration of the source by target windows and normally must be calibrated using a potential divider. Equally, they are unable to reach the measurement criteria given above.

In response to this problem, the Quantum Metrology Division at the National Institute of Standards and Technology (NIST) has proposed, developed, tested and patented a flat crystal spectrograph [3]. This is a Laue spectrograph with photographic detection, adapted from the earlier design by Rutherford and Andrade [4]. In

principle and experiment, ideal sources can be dispersed and focused with adequate precision to fulfil readily the sub-kV requirements. In practice, the source width broadens and obscures the required information, creating a potential problem. However, use of a curved crystal is able to overcome this limitation.

### The flat crystal spectrograph

The flat crystal spectrograph is illustrated schematically in Figure 1. X-rays from a point source will undergo attenuation and transmission through the crystal, but these direct lines of sight are shielded from the detection region. Hence only scattered X-rays can reach the detector. Incoherent scattering and specular reflection from surfaces are shielded from the detector by use of a collimating slit in front of the detection region. The slit location is chosen so that the distance from the point source to the crystal centre is equal to the distance from the crystal centre to the slit. The crystal is aligned in the Laue geometry, so that diffracting planes of interest are normal to the crystal surface as indicated in Figure 1.

Then the Bragg condition for coherent scattering (diffraction) is given by

$$\lambda = 2d \sin \theta \quad (1a)$$

$$E = q_e V = hc/\lambda \quad (1b)$$

where  $\lambda$  is a wavelength in the spectrum from the source,  $q_e$  is the charge on the electron,  $d$  is the interplanar spacing of the crystal,  $E$  is the corresponding energy of the radiation, and  $\theta$  is the diffracting angle. With alignment of the diffracting planes as suggested, radiation diffracted from any central region of the crystal (normal to the surface) is diffracted through the slit to reach the detector. Each wavelength of the source spectrum produces two images on the detector separated by a

---

Received 25 September 1995 and in final form 29 February 1996, accepted 28 March 1996.

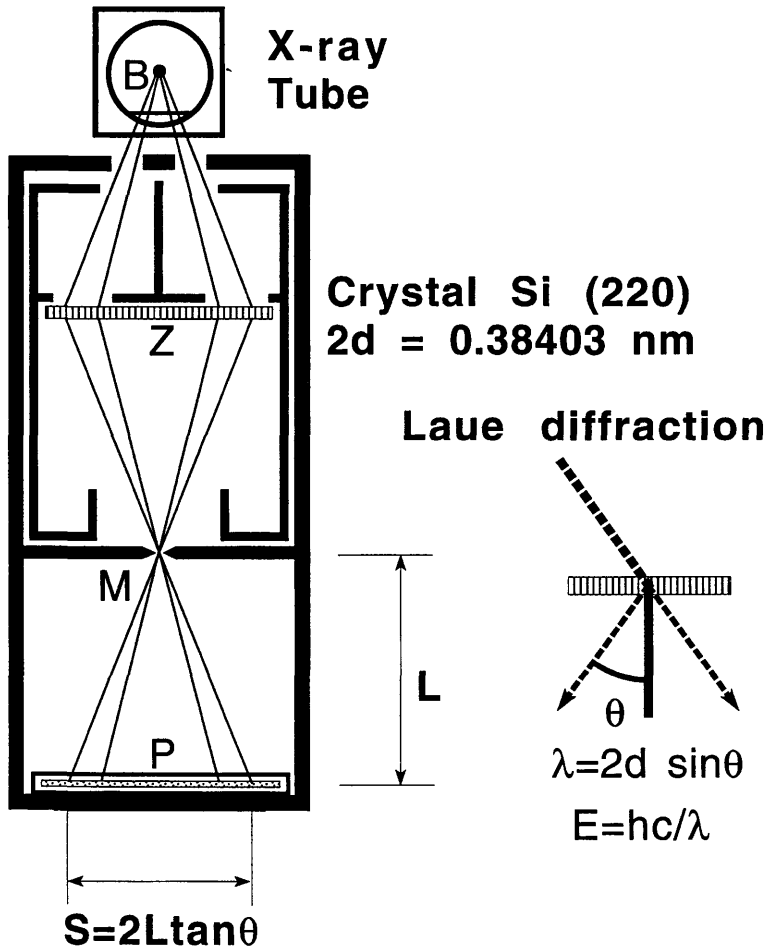


**Figure 1.** Flat crystal, symmetrical Laue spectrograph. A point source is imaged by Laue diffraction through a slit and onto a detector plane. The Bragg condition for Laue diffraction is illustrated on the side.

distance

$$S = 2(X - X_0) = 2|ZP - BZ| \tan \theta \quad (2)$$

where  $X$  is the distance of the image offset from the axis defined by the densitometer (the measured distance) and  $X_0$  is the central axis defined by the source and the diffracting planes.  $B$  is the source location,  $Z$  lies on the central plane of the crystal, and  $P$  is the point on the detector and the source-diffraction plane axis.

For a given operating voltage  $V$  of the X-ray tube source, the maximum photon energy  $E = q_e V$  corresponds to photon emission with the full energy of the incident electrons. This high energy limit of the continuous spectrum (the end-point energy) may be used to determine the effective operating voltage, given the numerical constant  $hc/e$  (known to high precision [5]), the interplanar spacing  $d$ , and the length ratio  $(X - X_0)/|ZP - BZ|$ . Rather than direct metrology, this is determined by calibration from accurately known characteristic emission lines of the tube source. Two unknowns would require two emission or edge energies, or three observed lines to determine the scaling. However, the diffracting crystal is chosen so that the

interplanar spacing is well defined, so that only one energy or two lines are sufficient to provide the calibration. There are usually two resolved emission lines in the range of energies imaged on the detector, so the system becomes suitably overdetermined.

The flat crystal prototype used a silicon crystal with 220 diffracting planes aligned as described, with an unstressed crystal spacing of  $d = 0.19201547(2)$  nm at  $T = 22.5^\circ\text{C}$  [6, 7]. Some experimental details are provided elsewhere [3]. Detection used standard Kodak DEF-392 X-ray photographic emulsion with routine development and imaging using an LKB scanning densitometer (see Appendix 3). Although effective, neither of these devices was critical to the results. Each densitometry trace used an aperture of 0.05 mm in the dispersion direction, integrating over 0.8 mm in image length, with step lengths in the dispersion direction of 0.02 mm (overlapping), and in the transverse direction of 0.8 mm (non-overlapping). Up to 10 traces of any given film would be taken. Image analysis allows each scan to be registered to a common channel prior to summation or averaging, to improve overall statistics and reduce noise due to background, dust or other (imaging) defects. For a

typical  $|ZP - BZ|$  distance of 100 mm, a voltage change from 20 kV to 30 kV leads to a contraction of the interval between left and right images of the end-point energy by 10 mm. Hence measurement of this distance and the scaling to within 0.1 mm establishes the X-ray tube voltage with an uncertainty of approximately 0.1 kV.

A typical spectrum is given in Figure 2. The molybdenum  $K\alpha_{1,2}$  line on each side, together with the

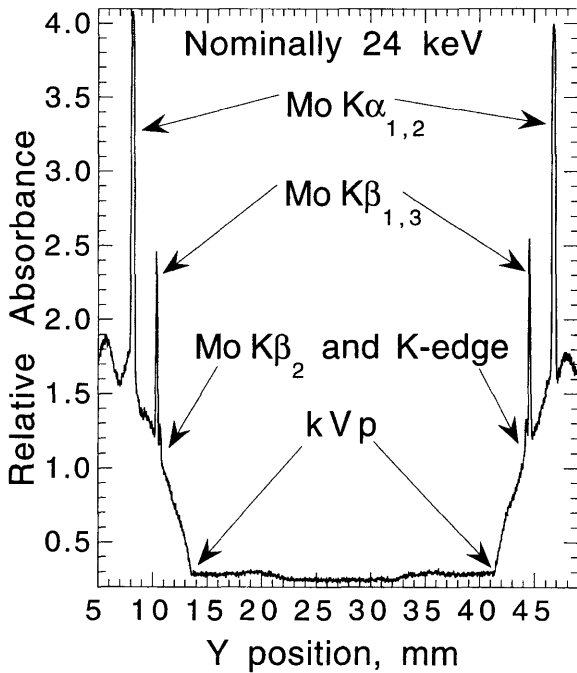


**Figure 2.** Typical densitometered spectrum from photographic emulsion located on the detector plane of the flat crystal prototype. Nominal tube voltage = 24 kV. Si 220 lattice used for Laue planes, of thickness 0.24 mm. The energy scale needed can be established either by length metrology or by reference to characteristic X-ray lines.

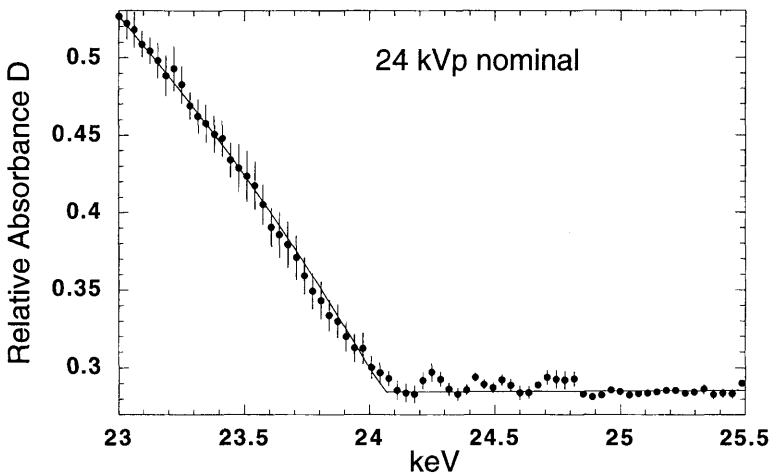


**Figure 3.** An expanded view of one image of the end-point region obtained using a nominal tube voltage of 24 kV. Data points are densitometry readings; the error bars represent the standard deviation of the distribution of readings from the region of uniform density. The straight line plus quadratic results from a fit of the edge location and coefficients in a least-squares sense for the photometric data in the background and continuum regions. The intersection of these two lines corresponds to the end-point energy and hence the X-ray tube voltage.

molybdenum  $K\beta_{1,3}$  line and the high-energy limit, form the basic data used to calibrate the spectrum and derive the high-energy limit. Because of the simple plate function, the axis may be recast directly into energy units, as indicated in Figure 3, where the end-point energy is specified with an appropriate 0.1–0.2 kV precision.

Errors and uncertainties explicitly include uncertainty in the location of the calibration lines and that of the edge. The assignment of densitometer or photographic error bars in the figure follows a simple overestimate based on the non-smoothness of the data (assuming an absence of structure).

**Assumptions and difficulties of the flat crystal method**

*Ray tracing*

A simple ray tracing routine or a direct geometric expression (as given above) can be used to model the flat crystal profile. These may be good approximations but are never exact and do not follow from detailed dynamic diffraction. Laue diffraction through an optically thin crystal does not have the angular profile of a delta function. Instead, the profile will display features given in Figure 4, from more detailed theory [8–10]. The oscillations are dramatic and the phase of interaction depends critically on the thickness. The thickness also allows diffraction loosely from Bragg planes near the front or rear surface of the crystal. These paths will interfere, but will also “trace” through to different locations on the image plane.

*Detector angle misalignment*

Perhaps more importantly, possible aberration or misalignment has not been considered. The simplest type is a misalignment of the detector plate at an angle  $\alpha_1$  to the normal for the diffracting planes. This results in a compression of features on one side of the plate ( $X_+ - X_0$ ), with an expansion towards the other side ( $X_- - X_0$ ). Here the paired line separation is

$$S = (X_+ + X_- - 2X_0) = |ZP - BZ| \sin \theta [1/\cos(\theta - \alpha_1) + 1/\cos(\theta + \alpha_1)] \quad (3)$$

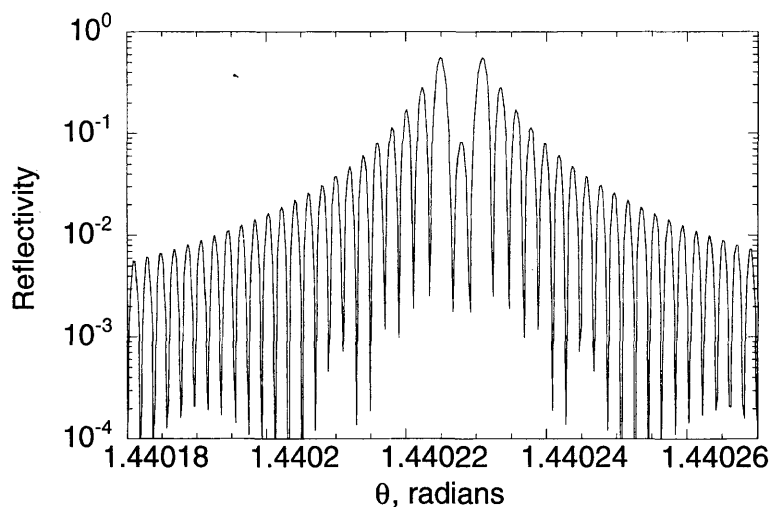


**Figure 4.** Actual Laue diffraction pattern for point source, monochromatic incident radiation (24.8 keV energy diffracting from Si 220 planes through a 0.1 mm thick crystal), as a function of diffracting angle in output profile, as would be observed at the image plate.

The offsets are not equal, so measurement of the end-point energy from the midpoint of two calibration lines is not a robust procedure.

#### Detector angle normal to dispersion axis

Deviation of the detector angle or alignment normal to this plane results in lines of features sloping towards the point of closest approach of the detector plate plane to the source. The relation for ideal alignment is still hyperbolic, but with zero slope. For a lateral offset  $X_Y$  from this ideal, corresponding to an angle subtended at the source  $B$  of  $\alpha_Y$ , given by  $\cos \alpha_Y = 1/\sqrt{[1 + X_Y^2/(BZ + ZP)^2]}$  the relation is

$$S = 2(X - X_0) = 2|ZP - BZ| \tan \theta \sqrt{[1 + X_Y^2/(BZ + ZP)^2]} \quad (4a)$$

For the non-ideal case where the plate and crystal planes subtend an angle  $\alpha_2$ , this becomes

$$S = 2(X - X_0) = 2 \tan \theta [(BZ + ZP)/\cos \alpha_Y - 2BZ/\cos(\alpha_Y - \alpha_2)] \quad (4b)$$

While the modification represented by Equation (3) is exact, Equation (4) neglects possible effects of varying the azimuthal angle and the changing crystal boundary conditions. These effects are minor perturbations of the diffraction profile compared with the larger geometric effects discussed here.

The correct midpoint is obtained from the average of paired lines or at infinite energy. This misalignment only affects the overall scaling, so can be subsumed within an effective parameter  $L = S/(2 \tan \theta)$  for the mean (or scan) separation. The modified equation introduces no additional dependence upon  $\theta$ , so a least-squares fitting of the data and calibration lines will be insensitive to this error.

#### Diffraction plane misalignment

Another minor issue relates to crystal imperfections, and particularly the planes of interest being not normal

to the crystal surface but having an additional angle  $\alpha$ . Assuming that the plate is aligned with the diffracting planes, the first order effect yields a lateral shift of the plate images, and a scaling

$$S = 2(X - X_0) = 2|MP| \tan \theta \quad (5a)$$

$$MP = BP - BZ \cos \theta [1/\cos(\theta + \alpha) + 1/\cos(\theta - \alpha)] \quad (5b)$$

where  $M$  is the new slit location and the point where monoenergetic X-rays are refocused. The scale is affected in the calibration process, but the zero location remains well defined.

#### Source location

The source location is not an issue if all line and bremsstrahlung radiation arise from the same region of the anode. It can be a problem for old sources or non-uniform filters, however. The relation given shows that if the source for one energy range is located 0.2 mm further from the crystal ( $BZ$  and  $BP$  increase by 0.2 mm) then the image will be contracted by  $0.4 \tan \theta$  mm. This would lead to a direct error in the calibration and voltage determination. Equally, a lateral shift of 0.2 mm of the source location for one energy range would lead to a 0.2 mm shift sideways for the corresponding image.  $S = 2(X - X_0)$  would be unchanged, however, so that a use of corresponding pairs of calibration and end-point energy separations should resolve the difficulty.

#### Source and crystal size

A more serious difficulty relates to the source size and crystal thickness for a given monochromatic wavelength contribution. This resolution is linear with the size of the source image. A lateral size of 0.2 mm or a longitudinal shift by  $0.2/\tan \theta$  mm will broaden the image and spectrum by 0.2 mm. This has a serious effect on the precision of the voltage determination. A similar difficulty arises from crystal thickness. Neglecting the full diffraction profile, the location of  $Z$  is broadened by

approximately this thickness so that a  $0.1/\tan \theta$  mm thickness will lead to a 0.2 mm broadening. For thicker crystals, anomalous transmission leads to a fairly sharply peaked function which reduces this effect.

**Design criteria for the curved crystal spectrograph**

A curved crystal Laue spectrograph is illustrated in Figure 5. The main design criteria include a high reflectivity to focus enough X-rays across the spectral distribution to allow good statistics to be obtained for the calibration in a reasonable time. The detector plate separation should be small enough for the calibration lines to appear on both sides at reasonable production cost. The resolution should be high and the dependence of image location on source position should be small. Optimization can proceed by detailed dynamic diffraction computation for selected cases (following [8, 9]), but many of the most important parameters may be addressed using relatively straightforward ray tracing, or preferably using approximate analytic formulae (following [10]).

*Diffraction*

This design uses curved crystal “backward” or “double-diffracted” Laue diffraction to produce the focused spectrum, while the “forward diffracted” beam is explicitly blocked by collimating slits. Further, the crystals operate in the “thick crystal” limit, so these two beams are well defined and well separated. This avoids unnecessary complication of the spectral pattern.

*Resolution*

The minimum width and hence maximum resolving power with a monochromatic source increases with Bragg angle or wavelength due to off-axis aberrations. Near the optimum focus, the widths increase almost linearly with crystal thickness  $T_c$ , indicating the inexact focus and a similar effect to that for the flat crystal imaging. This is indicated in Table I for dynamic diffraction from perfect Si 220 planes with a large 0.4 mm full width half maximum (fwhm) source truncated at  $\pm 0.3$  mm, at a distance of  $BZ = 150$  mm from the crystal.

Any choice of crystal and geometry must be tempered by possible broadening and structure widths in the source or final spectrum, and by limiting detector resolution. Although X-ray film is capable of 0.003 mm resolution, natural linewidths are typically 0.01 mm for molybdenum  $K\alpha_1$  (the most important structure for most mammographic calibrations), corresponding to a 7 eV width; while densitometry currently used proceeds in 0.02 mm steps with a slit broadening of up to 0.05 mm. Electronic detection (in readily available forms of an adequate size) is usually broader still. Hence the use of approximately focused curved crystals is quite adequate to achieve the qualitative improvement in resolution

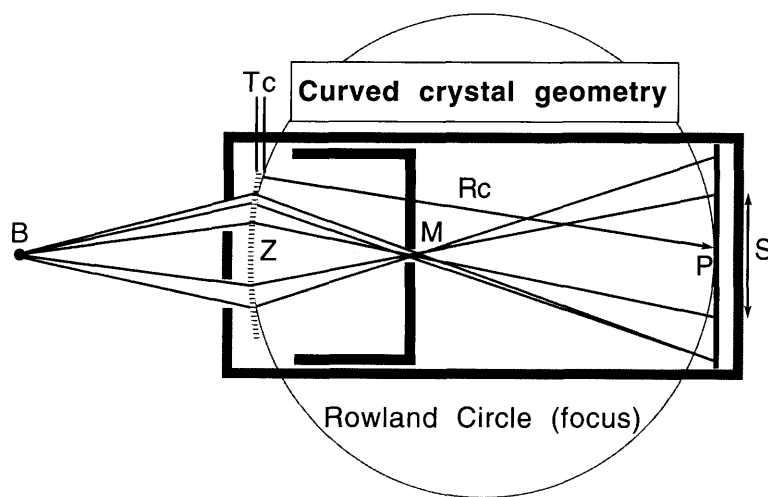


**Figure 5.** Laue spectrograph with curved crystal focusing, indicating Rowland Circle for focusing condition.

**Table I.** Simulated effect of crystal thickness on monochromatic full width half maximum linewidth (*i.e.* on resolution) for a range of energies, using Si 220 planes,  $PZ = 300$  mm

Energy	41.3 keV	31.0 keV	24.8 keV	17.7 keV	Limitation
Flat crystal	0.4 mm	0.4 mm	0.4 mm	0.4 mm	Source width
Curved crystals $R_c = 400$ mm	0.058 mm	0.053 mm	0.060 mm	0.064 mm	Defocused, source limited
$R_c = PZ$ , $T_c = 0.5$ mm	0.022 mm	0.028 mm	0.031 mm	0.042 mm	Diffraction or attenuation
$T_c = 0.1$ mm	0.009 mm	0.012 mm	0.018 mm	0.027 mm	Thickness limited
$T_c = 0.05$ mm	0.005 mm	0.007 mm	0.010 mm	0.016 mm	Thickness limited

required, and there is no demand to make the crystals unstably thin. The overall problem of flat crystal imaging with large sources or thick crystals can therefore be avoided.

**Reflectivity**

The second priority in this development is to increase the reflectivity uniformly over the energy range of interest, so that shorter detection times may be used in the calibration procedure. Curvature normally increases integrated reflectivity by allowing more crystal planes and regions to interact and diffract, and by reducing the lamellar thickness of the coherent unit (this is similar to the reflectivity increase for increasing crystal mosaicity). This is indicated in Figures 6–8. Peak reflectivity will usually decrease, at least in the local surface region of the crystal, although the geometric focusing can often reverse this effect at the focal plane. Curvature to an optimum radius typically increases reflectivities by a factor of 3 to 6. The reflectivity is weakly dependent on the source and detector locations, but the main concern

is the efficiency across energy with different radii. Figure 6 indicates that radii smaller than 200 mm are not suited to energies below 20–23 keV, for example.

A similar trend is obtained with increasing thickness. The optimum is determined by the increasing attenuation of thicker curved crystals, and the incoherence of highly curved lamellae (that is, the peak reflectivity continues to decrease but no additional regions become significantly diffracting). While low energy photons are greatly attenuated at large thicknesses (Figure 7, Si 220 diffracting crystal), this should not eliminate the precision of determination of calibration line centroids. Significant differences in reflectivity arise for the same thickness, and a focused detector location, but with different radii. The optimum parameterization and functional dependence vary significantly with crystal type or diffraction planes, as shown by comparison of Figures 7 and 8 (Si 111 diffracting planes). These integrated reflectivities include geometric losses for a cylindrical integration, following standard convention [8, 9].

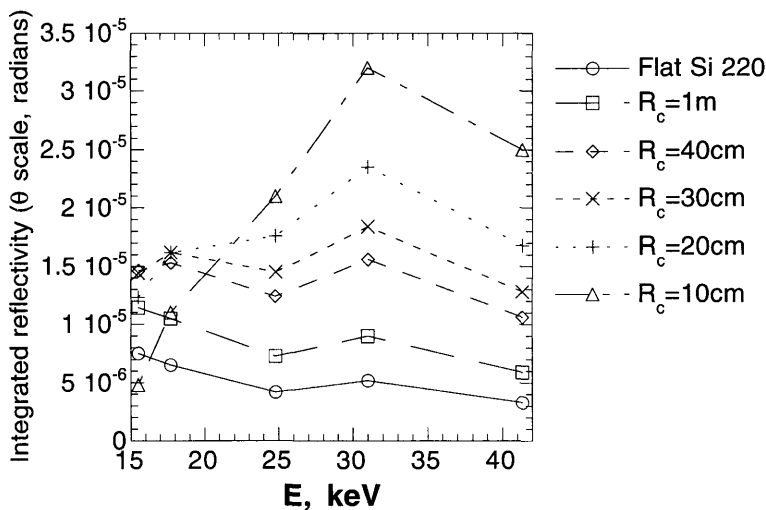


**Figure 6.** Integrated reflectivity *versus* curved crystal radius for diffraction of Si 220 planes with source-crystal distance  $BZ = 150$  mm, crystal-detector distance  $PZ = 200$  mm, and crystal thickness  $T_c = 0.1$  mm.

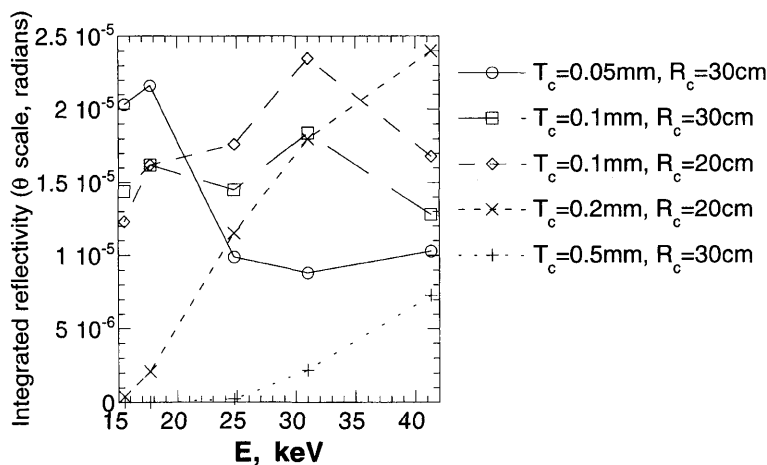


**Figure 7.** Integrated reflectivity *versus* curved crystal thickness  $T_c$  for diffraction off Si 220 planes with source-crystal distance  $BZ = 150$  mm, crystal-detector distance  $PZ = R_c = 200$  mm or 300 mm.

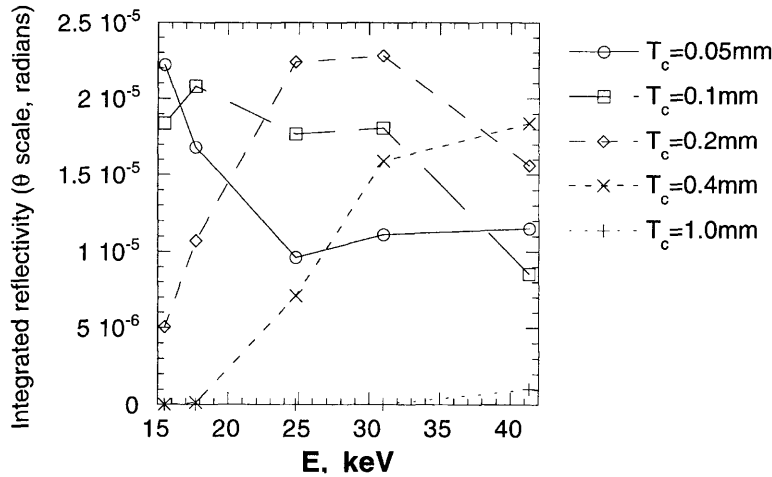


**Figure 8.** Integrated reflectivity versus curved crystal thickness  $T_c$  for diffraction off Si 111 planes with source-crystal distance  $BZ = 150$  mm, crystal-detector distance  $PZ = R_c = 200$  mm.

So far as the reflectivities and widths are concerned for the specific application of interest here, use of Si 220 crystal planes suggests crystal thicknesses  $T_c$  in the range  $0.2 \text{ mm} > T_c > 0.1 \text{ mm}$ , and radii of curvature  $R_c$  in the range  $300 \text{ mm} > R_c > 200 \text{ mm}$ . Conversely, use of Si 111 diffracting planes would suggest  $0.4 \text{ mm} > T_c > 0.2 \text{ mm}$  and  $200 \text{ mm} > R_c > 100 \text{ mm}$ . Technical difficulties of stressing crystals to these small radii can yield practical limits. The prime distinction between Si 220 and Si 111 lies in the relative 2D spacings of the lattice planes, leading to larger offsets and widths for Si 220.

*Curvature and detector plate location*

With ideal alignment of crystal planes, surface, collimating slit and detector plate, and negligible crystal thickness, with radius of curvature  $R_c$ , and assuming that the grazing Bragg angle is small so  $\sin \theta \approx \tan \theta$ , then the curved crystal plate factor is approximately

$$S = 2(X - X_0) \approx 2[(PZ - BZ) + BZ(BZ + PZ)/(BZ + R_c)] \sin \theta \quad (6)$$

If, in addition, the location of the plate is at the focus, so that  $PZ = R_c$ , then

$$S = 2(X - X_0) \approx 2PZ \sin \theta \quad (7)$$

This focal location is preferred and provides minimal fwhm on the detector plate for a given monochromatic radiation; and hence maximum resolving power. Hence  $R_c$  can be chosen simply, for a given spectrograph length and crystal.

Flat crystal spectrographs could be designed with the plate closer than the image slit location ( $BZ > PZ$  or  $MP < 0$ ). This gives compression of the plate image (financially desirable for electronic detection) but yields strong background and so is to be avoided. An equivalent curved crystal device (now involving  $R_c$ , so  $PZ \ll R_c$ ) would not be focused. In both crystal types the designs pictured are preferred. This implies that for a given  $PZ$  length, the offset  $X - X_0$  for a given energy will necessarily be larger in a curved crystal configuration. This can

enhance resolving power, but requires a larger spectrograph to image the same low energy structure.

Equations 6 and 7 indicate this focusing and scaling, but are inappropriate for use in spectrographic data analysis. Errors of these relations arise at the 3% level for Si 220, for calibrating lines, due to the inequivalence of  $\sin \theta$  and  $\tan \theta$ .

Conversely, dynamic diffraction and detailed ray tracing are both unnecessarily complex for the current application. Neither is readily invertible, as desired for efficient on-site analysis and calibration. Hence it is important to identify and criticise suitable approximate solutions to the problem.

**Defining equations for the curved crystal spectrograph**

The first step is to follow ray tracing assumptions and to assume that the crystal is negligibly thin and ideally cylindrical (noting particularly that increasing thickness did not have a dominant effect on the detected widths in the current regime in Table I). The alignment of planes, source and detector will be considered ideal. The result of this approach is given in Appendix 1, with parameters represented in Figure 9.

**Response of the spectrograph to defects**

The absolute accuracy attainable is a critical issue in this development. It is not adequate to test the device in a typical situation, it is also necessary to understand the

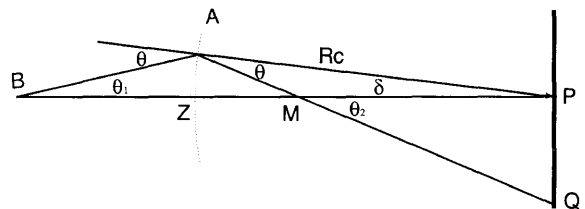


**Figure 9.** Curved crystal equation parameterization assuming point source and negligible crystal thickness.

type of errors or effects which may arise in less careful implementation, and to quantify these details. As some of the ideas have been presented above, this derivation will be discussed in Appendix 2 to allow readers to reach the conclusions more smoothly, and to then return to the necessary underlying details.

#### Experimental testing with X-ray sources: uncertainty and calibration

Focusing from Si 111 and Si 220 crystal planes has been investigated in detail for the prototypical devices illustrated in Figure 5. Significant uncertainty arises from photographic exposure, development and densitometry. For low optical densities, oscillations, aliasing and inconsistencies from these sources can be maintained to lower than 0.01 in optical density units (or relative absorbance). For densities above 1, and approaching the useful maximum of the densitometer around 3.6, these effects increase to around 0.1 in optical density. This uncertainty represents a limitation from statistics and reproducibility, but need not affect located centroids or calibration results at a severe level.

Estimates of limiting density precision can be based on theory [11] but in the current context two alternate simple empirical procedures were used to derive input channel error estimates for subsequent fitting. Each densitometer scan used a slit height of 0.8 mm. The central region of the exposed region of film was typically 5–10 mm in height. Hence a given photographic exposure may yield from five to 12 scans of independent data. Each densitometer scan yields a profile of peaks and the end-point energy, and these may be combined using the strong calibration lines to determine any variation of offset or scaling [3]. Statistical imprecision is then estimated by considering variation either between adjacent scans or along an individual scan. These estimates take account of random noise, emulsion holes and relatively rapid fluctuations, but also include variation from narrow line or edge structure. Hence they will generally overestimate the uncertainty in the data.

#### Linewidths and x-coordinate

The current analysis was based on fitting peaks of optical density *versus* energy, as opposed to transforming the data to intensity profiles. The latter is more rigorous but less convenient for a simple field exercise (as with routine mammographic voltage determination). The differences for the emulsion used and density–energy range observed are unlikely to yield significant error from this simplification. Linewidths in intensity space can correspond to values of density reduced from the peak by 0.3 (in the logarithmic range of the relation) and this width agrees with the slit width of 0.05 mm. This width is two to three times the natural linewidths and the ideal diffraction widths of monochromated radiation, so the contributions to widths and lineshapes appear well understood and in good agreement with predictions.

#### Resolution

One of the major improvements of the curved crystal approach is seen in Figure 10, taken with photographic

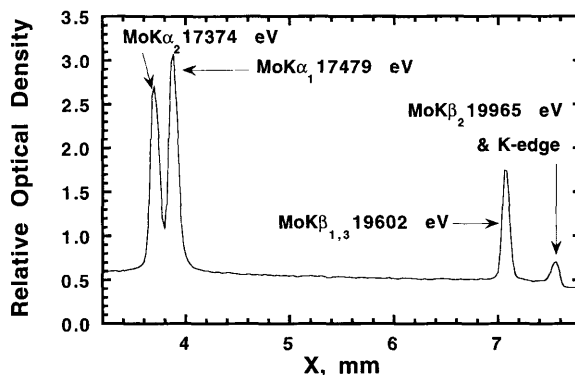


**Figure 10.** Curved crystal image of one set of the four molybdenum K calibration lines for a nominal tube potential energy of 26 keV, described in the text. The  $K\alpha_1$  and  $K\alpha_2$  components are well separated and the  $K\beta_2$  peak is clearly defined, even with broad sources, as opposed to flat crystal diffraction.

detection. The molybdenum  $K\alpha_1$  and molybdenum  $K\alpha_2$  lines are now clearly separated, as opposed to flat crystal diffraction. Another qualitative improvement is the identification and separation of the molybdenum  $K\beta_2$  peak as compared with the molybdenum K-edge at slightly higher energies. The optical density contrast of the former increases with increasing energy or exposure, and is typically 0.7–0.9 above a bremsstrahlung background of 0.5 (below the K-edge) and 0.4 (above the edge).

This allows eight calibration points to be used to determine the energy scale, instead of just four. The flat crystal function only required two points for the two parameters (neglecting defect variables), but the curved crystal formulae require four points, of which only one paired set provides independent information regarding  $X_0$  and an overall scale. Hence use of just a pair of  $K\alpha_{1,2}$  unresolved doublets and another pair of  $K\beta_{1,3}$  peaks is not adequate to determine a curved crystal scale. Having the additional well resolved and well defined peaks determines  $X_0$  much more precisely, is able to estimate magnitudes of misalignment variables from the overall consistency, and is able to determine (and overdetermine) the independent parameters.

Within these formulae, assumptions may be made regarding the alignment of crystal and detector ( $PZ$  and  $R_c$ ), in which case the formulae simplify, and three points are required [12].

The main calibration data discussed here used a 5 mA beam for 1–4 min exposure on a Si 111 crystal, with a  $0.3 \text{ mm} \times 0.3 \text{ mm}$  X-ray source at nominal energies from 22 keV to 40 keV in 2 keV steps. Fitted parameters used either quartic or quadratic formulae, with calibration lines and a peak-finding formula optimized for photographic data. The peak-finding routine is relatively crude and uses simple background subtraction (to be addressed in a subsequent paper).

### Line location accuracy

The calibration line locations are estimated to have an accuracy of about 0.15 channels for the  $K\alpha$  doublet and about 0.6 channels for the  $K\beta$  lines. In particular,  $K\beta_{1,3}$  is unresolved and  $K\beta_2$  is almost coincident with the K-edge, so that the K-edge line and background structure have greater uncertainty. Each channel has a step-size of 0.02 mm or about 20 eV, 31 eV, 49 eV or 67 eV at 22 keV, 28 keV, 34 keV or 40 keV energies. An alternate estimate of 0.3 channel uncertainty for all lines yields similar reduced  $\chi^2$  values of 1–5. A modified estimate of  $K\beta$  uncertainty of 0.75 channels was found to give significant variation in fitted parameters and individual end-point energy evaluations, but to have little effect on the overall average and generally to produce less reliable data. Hence the estimated accuracies are confirmed by the resulting fits and statistics.

### End-point locations

End-point locations are fitted separately with a linear background and a quadratic dependence near the end-point. Reduced  $\chi^2$  values of those particular fits are also typically 1–2 (confirming the densitometry channel error estimates) and yield correlation coefficients of  $R=0.99$  over 200–400 channels of data, and end-point location uncertainties of 0.25–1.0 channels, increasing to 1.75 channels for poor fits with significant noise and weak end-points at high energies (38 keV–40 keV). The end-point location is much harder to quantify than the calibration line locations, as is reflected in the relative uncertainties.

Fits of the end-point location are not particularly robust (in this sense) and depend significantly on the range used. For example, fits of the first end-point of the 28 keV data with 5.5 mm or 6 mm ranges and uncertainties based on consistency between scans (H) or within a scan (V) yielded values of  $15.817 \pm 0.011$  mm,  $15.784 \pm 0.005$  mm,  $15.797 \pm 0.012$  mm and  $15.761 \pm 0.005$  mm, thereby displaying variation up to four times the derived fitted uncertainty. In other cases, the local scatter agreed with the fitting uncertainty. A more reliable estimate of the final uncertainty is to use the derived energies (including uncertainties of calibration line energies) from a range of such reasonable schemes and compare the scatter observed.

Uncertainties are propagated to estimate the precision of determined energies. Derived uncertainty for an individual end-point with a particular channel weighting scheme is usually dominated by the scatter between different schemes or between the pair of end-point determinations.

### Nature of fitting results

Equation (8) in Appendix 1 was used to fit the derived calibration line locations and energies in two major modes. The first used a modified Levenberg–Marquardt routine, while the second included a more extensive grid-search and singular value decomposition approach (in addition). Reduced  $\chi^2$  values, parameter errors and derived energy uncertainties of both methods were usually very similar. The second method always improved the  $\chi^2$  value by a small but significant factor. In either

method, correlation is minimized by expressing  $R_c$  in terms of the more independent  $BZ/(BZ + R_c)$ . Both methods yielded typical uncertainties in  $R_c$ ,  $BZ$  and  $PZ$  of 20 mm, 5 mm and 5 mm, respectively. Conversely, the offset  $X_0$  is well defined to 0.002 mm or better. This result is a partial consequence of the function and parameter correlation with noise.

In the simpler mode of analysis, results returned values of  $R_c$ ,  $BZ$  and  $PZ$  in very good agreement with the mechanically measured parameters  $R_c = 250$  mm,  $BZ = 150$  mm,  $PZ = 250$  mm. This was convenient to establish the effect of an ideal relation. It was not the result of the improved fit, which typically shifted parameters by more than the returned uncertainty. This appears a systematic effect in that results of the simpler analysis yield a mean end-point energy some 100 eV–150 eV lower than the more extensive minimization. Both results appear systematically and significantly lower than results using quartic formulae.

### Quartic evaluation

Use of Equations (9–13) required the more extensive fitting process to disclose a reliable minimum. In this case, correlation was reduced by expressing  $BZ$  as the more independent parameter  $1 + BZ/R_c$ . Uncertainties of  $R_c$  were reduced to approximately 0.05 mm, while uncertainties in  $PZ$  were reduced to around 0.2 mm. Values of both parameters are in good agreement with the measured values, even after full minimization.

The returned uncertainty of  $BZ$  (and the value itself) via the parameter indicated above is very imprecise, corresponding to  $\pm 20$  mm or more. This arises from the nature of the curved crystal arrangement, which is explicitly insensitive to the source location B. Hence this result is a confirmation of the utility of the equations. The X-ray source is not a point source, whereas the formulae make that assumption. The inadequacy of that assumption has negligible effect on the crystal curvature  $R_c$ , the detector location  $PZ$ , or the film offset  $X_0$ , but has a large effect on the perceived source location  $BZ$ .

### Summary of uncertainties

The uncertainty of measured parameters (especially  $BZ$ ) has a minor effect on derived energies. Derivations using measured parameters directly (without fitting), or using uniform 0.3 channel weights in the fitting process, shift the located energies by less than one standard deviation. Unlike the use of Equation (8), the quartic fitting procedure appears robust. Additionally, we would expect the quartic approach to be improved on theoretical grounds and to yield physical parameters (as observed). In light of this confirmation, only results of quartic fitting shall be presented.

Uncertainties of intensity and density measurement do not provide a serious constraint of overall precision, but a great utility of the curved crystal approach lies in the enhanced resolution and hence calibration of the end-point energies.

### Analysis and results

A consequence of the quartic equations having lower parameter uncertainty than the quadratic approach is

that the derived end-point energies also have lower uncertainty. The scatter between end-point determinations using different error estimates (H between scans, V within each scan, or L for a linear estimate) is similar and dominates over final error estimates. The major contribution to the uncertainty of an individual end-point energy is the local fitting error, with a smaller contribution from the quartic fit and extrapolation from calibration lines, and minor contributions from energy uncertainties and background considerations in calibration lines. Figure 11 indicates the derived end-point energy for a single error scheme (V), the first edge (1) and the nominal 22 keV energy. Fitting precision is 10 eV, although this increases with local noise and with energy, and the scatter between fits is much larger than this.

The overall result may be seen in Figure 12. The difference in energy between measured end-point energies and the nominal value from the dialed source voltage is plotted against the nominal voltage. Three error schemes and two end-point energies provide five sets of

measurements, as indicated. The first three (1 H, 1 V and 2 H) are given error bars to illustrate individual fitting precision and the precision of the calibration. These error bars increase with energy as the energy scale is compressed and the relative noise increases. Particular schemes fail occasionally but obviously—as exemplified by  $E_{1V}$  (30 keV) and  $E_{2V}$  (36 keV). Inspection of fitted profiles for these points proves that the fit in question has failed. For low energies (22 keV–28 keV) the V scheme yields more consistent results; while for higher energies the H and L schemes are more robust. Two measurements were plotted for 30 keV; the second used a different crystal but produced a very similar average result (neglecting the outlier). Overall scatter is below 100 eV for lower energies, but rises above this value at high energies.

Results of these photographic trials indicate an error of the nominal voltage of the source observed of approximately 200 eV at low energies (22 keV) rising to about 400 eV at high energies (40 keV), or a scale error of approximately 1%. Additionally, the first edge is

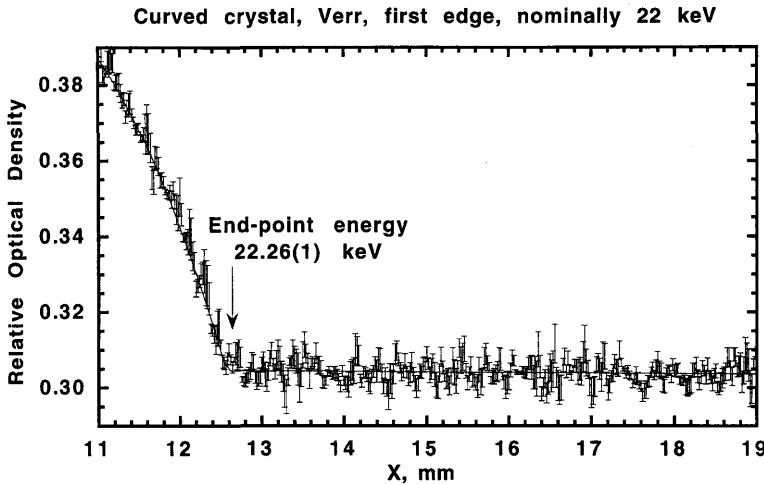


Figure 11. Detail of individual curved crystal end-point determination indicating channel uncertainties derived from scatter with a scan, for the first end-point of the pair ( $E_{1V}$ ), and a nominal source voltage of 22 kV. Each datum represents a step width of 0.02 mm or 20 eV. Below the endpoint, a quadratic dependence of density upon energy is assumed; above the endpoint, the background is assumed to be linear.

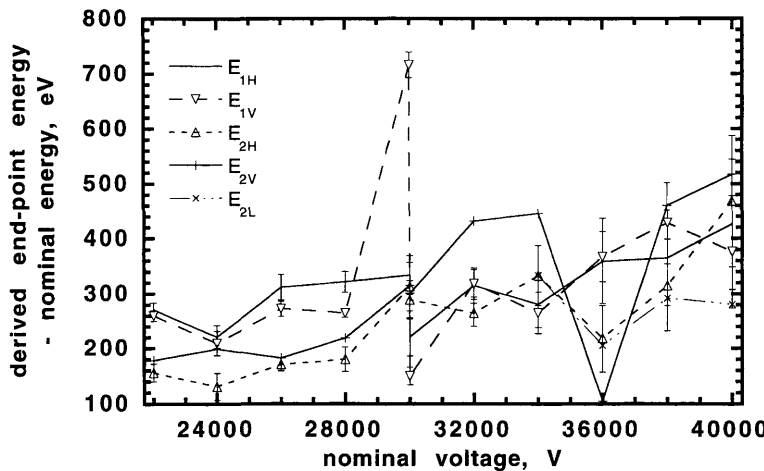


Figure 12. Overall display of derived end-point energies from the set of nominal energies with the curved crystal prototype. Error bars are indicated on the first three sets. The first or second derived end-point energies are labelled ( $E_1$  or  $E_2$ ) with a subscript indicating the source of the channel uncertainty used (H for the scatter between scans, V for the scatter within a scan, or L for a uniform linear estimate). Occasional errors are observable, but the strong trends have a small uncertainty.

predominantly higher in derived energy than the second, in all schemes, indicating the magnitude of a misalignment following Equations (14) or (15). These are errors of the nominal voltage and alignment, and not of the X-ray method.

### Conclusions and application

The mean results at each energy follow a reliable trend with an uncertainty at or below 100 eV. To this 100 eV uncertainty should be added 100–200 eV in quadrature for the sum of (unquantified) misalignment defects of a particular crystal. Even so, this is well within the calibration accuracy required for screening centres. Hence a precision of at or below 100 eV is achievable, with an accuracy of better than 500 eV.

This paper has demonstrated a number of developments and modifications, but detector technology and crystal modifications have been neglected and are the subject of a separate study [12]. Observed noise and routine exposures are not unreasonable in the curved crystal devices discussed in this paper. Important developments are, however, required towards more routine non-invasive calibration of voltage supplies *in situ*. These are discussed elsewhere, particularly with a view to clinical conditions and filtering [12]. Two basic routes appear open to further investigation and trials. One involves the type of device indicated here as a low-cost approach in countries with limited budgets or facilities; while a more attractive alternative for developed sites and countries would involve superior and automated detection and processing. These devices would be applied directly to clinical units for *in situ* non-invasive tube potential measurement, following initial calibration, without any other intermediate.

Tests of these devices under clinical conditions with screening X-ray sets in screening centres have been made [12] and the results are fully in agreement with the uncertainties and errors discussed above. The method has been proven to be a successful new non-invasive technique for mammographic voltage determination to high precision and accuracy. It should be clear that the results of this paper lay the groundwork theoretically for this new class of device. It also experimentally demonstrates an appropriate form for the low-cost approach. A more advanced detection method using the results and technique demonstrated herein, together with further details of the screening centre tests, will be presented separately.

### Acknowledgments

Dr Chantler would like to thank other members of the Quantum Metrology Division for helpful discussions and interaction, and the Division itself for the Visiting Researcher position during much of the period of this research.

### References

1. LAW, J, The measurement and routine checking of mammography X-ray tube kV, *Phys. Med. Biol.*, 36, 1133–1139 (1991).

2. DEPARTMENT OF HEALTH, *Revised Guidance Notes for Health Authorities on Mammographic X-ray Equipment Requirements for Breast Cancer Screening*, Publication STD/90/46 (HMSO, London) (1990).
3. DESLATTES, R D, LEVIN, J C, WALKER, M D and HENINS, A, Non-invasive high-voltage measurement in mammography by crystal diffraction spectrometry, *Med. Phys.*, 21, 123–126 (1994).
4. RUTHERFORD, E DA C and ANDRADE, E N, The spectrum of the penetrating g-rays from Radium B and Radium C, *Phil. Mag.*, 28, 263–273 (1914).
5. COHEN, E R and TAYLOR, B N, The 1986 adjustment of the fundamental physical constants, *Rev. Mod. Phys.*, 59, 1121–1148 (1987).
6. DESLATTES, R D and KESSLER, E G JR, Status of a silicon lattice measurement and dissemination exercise, *IEEE Trans. Instr. Meas.*, 40, 92–97 (1991).
7. SCHWEPPE, J, DESLATTES, R D, MOONEY, T and POWELL, C J, Accurate measurement of Mg and Al  $K\alpha_{1,2}$  X-ray energy profiles, *J. Elect. Spect.*, 67, 463–478 (1994).
8. CHANTLER, C T, X-ray diffraction of bent crystals in Bragg geometry. I. Perfect-crystal modelling, *J. Appl. Cryst.*, 25, 674–693 (1992).
9. CHANTLER, C T, X-ray diffraction of bent crystals in Bragg geometry. II. Non-ideally imperfect crystals, modelling and results, *J. Appl. Cryst.*, 25, 694–713 (1992).
10. CHANTLER, C T and DESLATTES, R D, Systematic corrections in Bragg X-ray diffraction of flat and curved crystals, *Rev. Sci. Instr.*, 66, 5123–5147 (1995).
11. CHANTLER, C T, Photographic response to X-ray irradiation. I: Estimation of the photographic error statistic and development of analytic density–intensity equations, *Appl. Optics*, 32, 2371–2397 (1993).
12. HUDSON, L T, DESLATTES, R D, HENINS, A ET AL, Current status and development of a curved crystal spectrometer for energy calibration and spectral characterization of mammographic X-ray sources, *Med. Phys.* (submitted).

### Appendix 1: Analytic defining equations for the curved crystal spectrograph

Following the introduction in the section “Defining equations for the curved crystal spectrograph” we present the solution using nomenclature introduced above and in the figures.

#### Quadratic approximation

The next step is to retain  $\tan \theta$  terms initially, but to assume that  $\cot^2 \theta \gg 2R_c BZ / (R_c + BZ)^2$ . Then the prior small-angle assumption is relaxed, to yield

$$X - X_0 \sim |PZ \tan[\theta + (BZ \tan \theta) / (R_c + BZ)] - BZ \tan[\theta - (BZ \tan \theta) / (R_c + BZ)]| \quad (8)$$

This neglects the shift along the vector  $BP$  from the crystal pole  $Z$  to the actual off-axis diffracting surface. For small Bragg angles, this is adequate. This solution corresponds to an analytical quadratic relation and is convenient. To address the question of whether this solution is adequate in the current voltage calibration, the “quadratic approximation” may be relaxed to a quartic approximation. Within the assumptions above, this solution is exact; relaxing the assumptions further is possible but would then have no analytic solution.

**Quartic approximation**

Following Figure 9, this yields the defining equations:

$$\begin{aligned} \theta_1 &= \theta - \delta, \quad \theta_2 = \theta + \delta, \\ PZ &= R_c(1 - \cos \delta) + QA \cos \theta_2, \\ X - X_0 &= PQ = |R_c \sin \delta - QA \sin \theta_2|, \\ R_c \sin \delta &= [R_c(1 - \cos \delta) + BZ] \sin \theta_1 \end{aligned} \quad (9)$$

or

$$\begin{aligned} \xi^4 + p\xi^2 + q\xi + r &= 0, \quad \xi = \cos \delta + B/4, \\ p &= C - 3B^2/8, \quad q = D + B^3/8 - BC/2, \\ r &= E + B^2C/16 - BD/4 - 3B^4/256, \\ (\cos^4 \delta + B \cos^3 \delta + C \cos^2 \delta + D \cos \delta + E &= 0), \\ B &= -2(\cos \theta + 1 + BZ/R_c), \\ C &= \sin^2 \theta + (1 + BZ/R_c)^2 + 2 \cos \theta(1 + BZ/R_c), \\ D &= 2[\cos \theta + (1 + BZ/R_c) \cos^2 \theta], \\ E &= -1 - 2(1 + BZ/R_c) \cos \theta - (1 + BZ/R_c)^2 \cos^2 \theta \end{aligned} \quad (10)$$

Then solving for  $\delta$  and matching the sign with that of  $X - X_0$  provides the image location relative to an offset  $X_0$  as

$$X - X_0 = [PZ - R_c(1 - \cos \delta)] \tan(\theta + \delta) - R_c \sin \delta \quad (11)$$

**Solution**

The parametric form of Equation (9) is simple but provides no analytic determination of  $X$  from  $\theta$  or of  $\theta$  from  $X$ , therefore invoking numerical derivatives to solve the problem. This is simpler than the full dynamic computation, but we shall bypass this method in favour of an analytic determination of  $X$  from  $\theta$ . The solution involves defining

$$\begin{aligned} f &= (q^2 + 2p^3/27 - 8pr/3); \quad g = f^2 - 4(4r/3 + p^2/q)^3; \\ \text{If } g \geq 0, \text{ then } \alpha, \beta &= f \pm 0.5\sqrt{g}; \quad t_0 = \sqrt[3]{\alpha + \sqrt{\beta}} + p/3 \end{aligned} \quad (12a)$$

$$\begin{aligned} \text{If } g < 0, \text{ then } \alpha &= 0.5\sqrt{(f^2 - g)}; \quad \beta = \text{acos}(f/\alpha); \\ t_0 &= p/3 + 2\sqrt[3]{\alpha \cos \gamma}; \\ \gamma &= \beta/3, (2\pi + \beta)/3, \text{ or } (4\pi + \beta)/3 \end{aligned} \quad (12b)$$

whence  $\xi$  is given by

$$\begin{aligned} \xi &= \{ \sqrt{(t_0 - p)} \pm \sqrt{[(t_0 - p) - 2(t_0 + q/\sqrt{(t_0 - p)})]} \} / 2 \text{ or} \\ \xi &= \{ -\sqrt{(t_0 - p)} \pm \sqrt{[(t_0 - p) - 2(t_0 - q/\sqrt{(t_0 - p)})]} \} / 2 \end{aligned} \quad (13)$$

A least-squares fitting procedure can derive  $\delta_n$  and hence  $PZ$ ,  $BZ$ ,  $R_c$  and  $X_0$  given values for  $X_n$  and  $\theta_n$  for the calibration lines. Then fitted end-point positions  $X_{E+}$ ,  $X_{E-}$  in image plane units (mm) can be used in an inverted iterative relation to provide  $\delta_E$  and  $\theta_E$ , and finally the end-point energy.

**Comparison of forms**

Assumptions are still being made here about the uniformity of surface, source and diffraction plane orientation (to be partially addressed later). The crystal thickness and intrinsic diffraction profile primarily broaden the result without confusing the calibration. A comparison of simple scaling formulae (Equation (2) for flat crystals and Equation (7) for curved crystals) is given in Figure 13 to indicate the image size and energy dependence for typical configurations. Compared to these values, Figure 14 indicates the inadequacy of using  $\sin \theta$  to approximate  $\tan \theta$  for the flat crystal relation at low energies. The analogous simplification for the curved crystals is much more significant because the plate function  $X$  (or the dispersion function  $dX(\lambda)/d\lambda$ ) is much larger and the relation is less well approximated.

However, the quadratic relation (Equation (8)) appears well behaved and parallel to detailed computations of  $\sigma$  or  $\pi$  polarized radiation including source widths and crystal thicknesses. It was then hoped that the simpler form would fit the molybdenum K spectra to adequate precision. However, the errors of order 1% appear sufficient to couple with the small set of calibration lines and distort the determination of the independent parameters. This could be due to correlations with noise, defects of the alignment, or the greater robustness of the quartic relation (Equations (9–13)).

**Appendix 2: The effect of spectrograph or alignment defects on calibration relations and possible inaccuracy**

Following the section ‘‘Response of the spectrograph to defects’’ and Appendix 1, we present the relations for the following defects.

**Detector angle misalignment**

The misalignment of photographic plate angle has a similar dependence to the flat crystal relation:

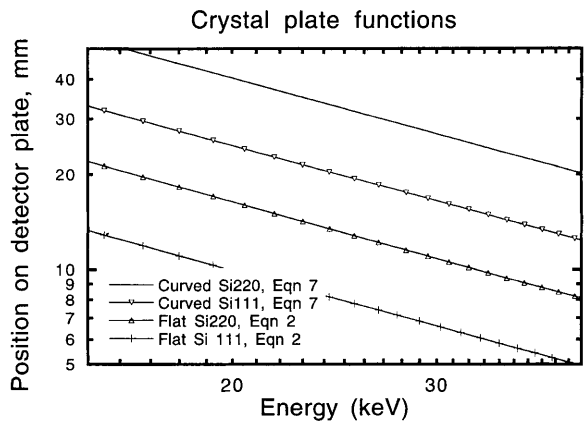


**Figure 13.** Crystal plate function  $X = PQ$ , mm, versus  $E$ , for  $BZ = 150$  mm,  $PZ = 250$  mm, and curved or flat crystals of Si 111 and Si 220 (using Equations (7) and (2)). The curvature increases the feature separation for any energy, and the scaling decreases with increasing lattice spacing.

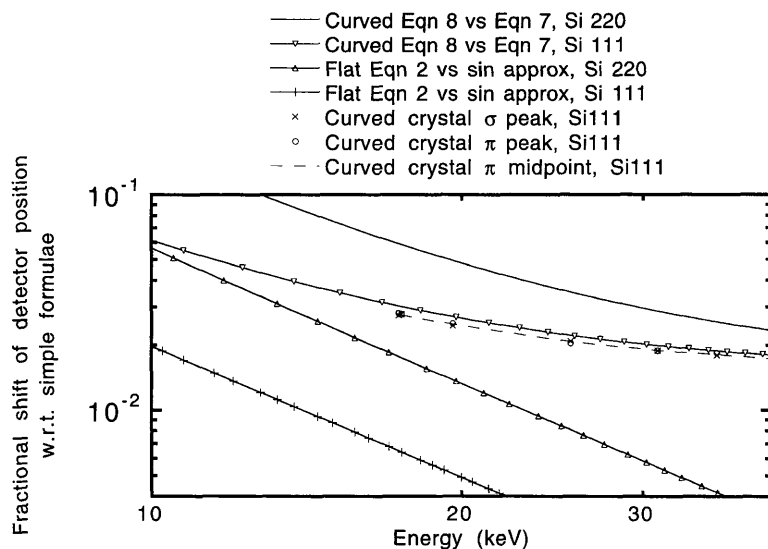


**Figure 14.** Fractional shift of lateral position *versus* energy as compared with simple Equations (7) and (2). While flat crystal corrections from the use of sin or tan functions remain small and follow parallel lines on this log-log plot, the curved crystal relations show larger effects and a stronger variation with energy.  $R_c = 240$  mm is used.

$$S = X_+ + X_- - 2X_0$$

$$= (X - X_0) \cos \theta_2 [1/\cos(\theta_2 - \alpha_1) + 1/\cos(\theta_2 + \alpha_1)] \quad (14)$$

As for the flat crystal, this is an asymmetric scaling with angle, so that compression and expansion are unequal and the midpoint of a given pair of lines does not yield  $X_0$ . An overall fit can determine  $\alpha_1$  as the parameter is largely independent of other scaling parameters. To first order and for small angles, any angle normal to the dispersion plane is treated similarly to the flat crystal Equation (4b), once again yielding a relation independent of  $\theta$  and  $\delta$  and hence only affecting the overall scaling parameter. Detailed diffraction computations show that this is not precisely true but is here an adequate approximation. Magnitudes of  $\alpha_1$  and  $\alpha_2$  can usually be constrained below  $7'$  corresponding to  $X_Y < 0.1$  mm at the centre of the detector plate. Diffracting angles vary from  $10.6^\circ$  for molybdenum  $K\alpha$  radiation diffracting off Si 220 planes, to  $2.8^\circ$  for 40 keV X-rays diffracting off Si 111 planes. In the example geometry, this corresponds to values of  $\delta$  from  $4^\circ$  to  $1^\circ$ .

#### Diffraction plane misalignment

Misalignment of diffracting planes leads to a symmetric scaling to

$$\theta_1 = \theta - \delta + \alpha, \theta_2 = \theta + \delta - \alpha \quad (15)$$

The remainder of Equation (9) is unchanged, but this modification requires rederivation of coefficients of Equations (10–11) for each side of the crystal (not given here). Further,  $\alpha$  is correlated with  $\delta$  and the scaling parameters and hence less amenable to derivation. This effect is energy dependent as for the flat crystal, but the information content in the calibration lines is usually unable to determine the value of  $\alpha$ . However,  $\alpha$  is typically aligned to better than one arcminute and often better than a few arcseconds for good silicon and germanium crystals.

Table II illustrates the shift of  $X_\pm - X_0$  locations for primary calibration lines and typical edge energies for the case  $R_c = 240$  mm,  $PZ = 250$  mm,  $BZ = 150$  mm. Defects of  $\alpha_1 = 7'$ ,  $\alpha_2 = 70'$ ,  $X_Y = 10$  mm, and  $\alpha = 2'$  are compared with the quadratic and quartic formulae to indicate typical magnitudes. While the shift of image

**Table II.** Effect of defects on Si 220 plate function (value of  $|X - X_0|$  in mm *versus* calibration or edge energy) for selected energies, with  $R_c = 240$  mm,  $BZ = 150$  mm,  $PZ = 250$  mm

Line	MoK $\alpha_2$	MoK $\alpha_1$	MoK $\beta_{1,3}$	MoK $\beta_2$	Edge?	Edge?	Edge?
$E$ (keV)	17.374	17.479	19.602	19.965	25.000	30.000	35.000
$ X - X_0 $ (mm)	48.783	48.470	42.922	42.101	33.312	27.623	23.607
Eqn (14), $\alpha_1 = 7', X_-$	48.810	48.496	42.942	42.121	33.324	27.632	23.613
$\alpha_1 = 7', X_+$	48.757	48.444	42.902	42.082	33.300	27.615	23.601
Eqn (4b), $\alpha_2 = 70', X_Y = 0$	48.753	47.440	42.895	42.075	33.291	27.606	23.592
Eqn (4a), $X_Y = 10$ mm	48.799	48.485	42.935	42.115	33.322	27.632	23.614
Eqn (15), $\alpha = 2', X_-$	48.933	48.620	43.071	42.250	33.458	27.768	23.752
Eqn (15), $\alpha = 2', X_+$	48.633	48.320	42.773	41.953	33.165	27.478	23.462

Mo, molybdenum.

location is significant at the level of energy uncertainties, the largest shift from the diffraction plane misalignment is still less than 0.1 keV for calibration lines and less than 0.21 keV for possible edge energies. This suggests that the tolerances indicated are necessary (within a factor of two) to achieve the desired performance, and that typical crystal alignments will be adequate. Although the quadratic formula gave similar results and dependences of  $X$  on energy to Equations (9–13), the optimized parameters become unphysical and will lead

to correlated errors in the fits. Equation (6) is much worse, and produces errors of 1–2 keV without introduction of noise. Hence the use of Equations (9–13) appears indicated.

### **Appendix 3**

This identification does not imply endorsement nor should it be taken to suggest that the identified items are necessarily best suited for the applications in which they are used.